PHYSICAL REVIEW B **66**, 085206 (2002)

Ultrafast dynamics in phosphorus-implanted silicon wafers: The effects of annealing

Andreas Othonos* and Constantinos Christofides
Department of Physics, University of Cyprus, P.O. Box 20537, 1678 Nicosia, Cyprus
(Received 1 November 2001; revised manuscript received 24 April 2002; published 19 August 2002)

Carrier relaxation in phosphorus-implanted silicon wafers (10^{16} P^+/cm^2) annealed at different temperatures ranging from 350 to 1100 °C is investigated by near-infrared ultrafast time-resolved reflectivity measurements. A kinetic model based on four couple differential equations describing the carrier density, electron, hole, and lattice temperatures is used to evaluate the expected changes in the time-resolved reflectivity. This model was used to fit the experimental data having the trap recombination time constant and the optical absorption coefficient as fitting parameters. Our measurements reveal a complicated recovery of the ion-implanted silicon samples to crystallinity following annealing with carrier lifetimes ranging from <1 psec for the nonimplanted sample and reaching ~95 psec for the highest-annealed sample. Although this recovery directly effects the lifetime of the carriers, there are nontrivial mechanisms that activate recombination centers and traps throughout the annealing process, resulting in carrier lifetimes that are shorter than expected at higher annealing temperatures. Raman scattering data demonstrate the disorder and the recovery of ion-implanted silicon to its crystalline form, offering a direct comparison to the time resolved reflectivity data.

DOI: 10.1103/PhysRevB.66.085206 PACS number(s): 78.40.Fy, 61.80.Jh

I. INTRODUCTION

The progress in microelectronics over the past two decades has placed an enormous demand in the process and control of semiconductor doping. This has inspired a great deal of investigative work, both experimental and theoretical, in the area of ion implantation and its effects in semiconductors. Ion implantation as a means of doping semiconductors offers many advantages, some of which are accuracy and control of the amount and range of dose and absolute control of the implantation region and profile.[1] However, despite the many advantages this process has to offer, there is one main drawback: namely, the damage induced in the semiconductor. Some of the results of these damages are amorphization of the semiconductor in the case of high ion implantation, the presence of point defects, interstitial impurities, dislocations lines and loops, gain boundaries, and inhomogeneities.[1] Annealing, therefore, must follow ion implantation, a process by which the damaged sample recovers its crystallinity and the doping impurity becomes electrically active. Thermal annealing itself results in various other problems such as redistribution of the impurity atoms,[2,3] which may cause serious problems in semiconductor devices. It is, therefore, important to study, in detail, ion implantation and the subsequent process of annealing, thus obtaining a better understanding and control of ion-implanted processed semiconductors.

The recent demand for high-speed microelectronic devices with ultrafast response has given a renewed interest in this area. Although crystalline silicon has a slow response, it is known that amorphous silicon[4,5] and amorphization due to ion implantation process[6] alter the temporal behavior in these materials. Amorphous silicon has been reported with an ultrafast response shorter than picosecond due to their short free-carrier lifetimes. The reduction of the free-carrier lifetime is the result of the introduction of defects into the crystalline semiconductor, which acts as traps and recombination centers.

It is well known that above the band gap, direct or indirect (e.g., phonon-assisted) optical excitation of semiconductors generates electrons and holes. The dynamics of these photogenerated carriers can be monitored directly using time-resolved reflectivity measurements.[7] The contribution of the carrier plasma to the reflectivity can be estimated using the Drude expression for the index of refraction.

Here we demonstrate the sensitivity of ultrafast time-resolved reflectivity measurements in highly implanted silicon to the various defects and redistributions of these impurities following annealing at several temperatures. The technique utilizes a pump pulse to excite carriers, which are monitored using a weaker probe beam through the changes induced in the index of refraction of the material. The variation in the index of refraction is monitored as change in the reflectivity, which is a direct measure of the photoexcited carrier lifetime and in effect a measure of the recombination traps in the noncrystalline silicon. Furthermore, using a kinetic model based on four couple differential equations describing the carrier density and temperature dynamics along with a reflectivity model, we were able to describe accurately the temporal profile of the induced changes in reflectivity. Finally, we were able to estimate, through a fitting process to our experimental results, the optical absorption coefficient for all annealed samples.

II. EXPERIMENT

The experimental setup is shown in Fig. 1. A solid-state laser (Millennia) was used as a pump source for a mode-locked Ti:sapphire laser (Spectra-Physics, Tsunami) tuned at 790 nm. The mode-locked oscillator produced 80-fsec pulses in duration. The experimental arrangement was used to separate the incident laser beam into a pump and probe beam. The pump intensity was set to 100 mW, whereas the probe was kept 100 times weaker (~1 mW). The optical elements in the experimental arrangement were carefully selected to have minimum dispersion effect on the optical pulse duration, thus maintaining maximum temporal resolution. The

 ©2002 The American Physical Society

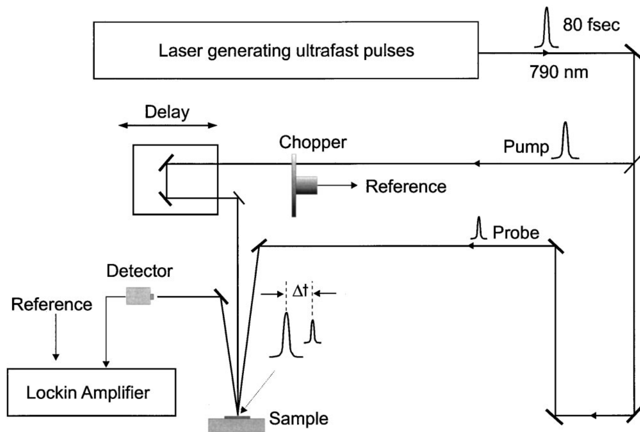

FIG. 1. Schematic diagram of the femtosecond, pump-probe, time-resolved reflectivity experiment used in this work.

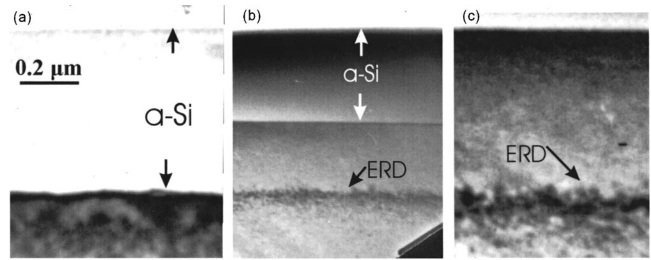

FIG. 2. Cross-section transmission electron micrographs from the phosphorus implanted silicon samples. (a) Implanted and nonannealed silicon sample showing the amorphous layer of approximately 0.55 μm. (b) A sample implanted and annealed at 500 °C which displays an amorphous layer of approximately 0.35 μm. (c) This is the completely recrystallized implanted silicon with the buried end of range defect (ERD) zone. This sample was annealed at 600 °C.

probe beam was focused on the sample to a spot that was 30 μm in diameter within the pump beam that was 60 μm in diameter. Alignment and elimination of the walk-off effect during optical translation of the two focus beams was achieved using a beam analyzer with submicron resolution. The relative angle of incidence to the sample of the two beams was less than 10°. The intensity of reflected probe light was measured with a photodiode, which was processed with a lock-in amplifier. Under the excitation condition of the experiment no apparent damage was induced on the samples. The major source of errors in the time-resolved reflectivity measurements was the small intensity fluctuations of the laser beam. However, the use of a solid-state laser pump along with the phase sensitive technique has allowed us to detect changes in the reflectivity less than several parts in 10^6.

The samples used in these experiments are silicon wafers lightly doped with boron (20–25 Ω cm) implanted with phosphorus at doses of 1×10^{16} P^+/cm^2 and implantation energy $E=150$ keV through a thin oxide layer at room temperature. After implantation the thin oxide layer was removed and wafers were cut along the crystallographic axes into several samples of dimensions 1×1 cm^2. These samples were then thermally annealed isochronically at various temperatures: 350, 400, 500, 600, 700, 800, 900, 1000, and 1100 °C for 1 h in an inert nitrogen atmosphere. Transmission electron microscope (TEM) measurements on these samples reveal an amorphous layer, which was approximately 0.55 μm thick for samples with annealing temperatures lower than or equal to 400 °C. Some representative cross-section transmission micrographs from the above phosphorous-implanted unannealed and annealed silicon wafers are presented in Fig. 2. The values are in good agreement with 1D-SUPREM III numerical simulations.[8] Measurements on the 500 °C–annealed sample display an amorphous layer of 0.35 μm, whereas no amorphous layer was noticeable for higher annealing temperatures, although some dislocation loops are noticeable. The diffusion of the implanted impurities was also measured in the past using spreading resistance measurements.[8]

The optical penetration depth of the pump and probe beams at the operating wavelength play a crucial rule in the experiments. For crystalline silicon the optical absorption is approximately 10^3 cm^{-1} corresponding to 10 μm excitation region. However, for the implanted samples the penetration depth is estimated to be a factor of 20 smaller.[9–11] In addition to the pump-probe time-resolved reflectivity experiments Raman scattering measurements at 752.5 nm were also performed on all the samples. These measurements will help in the analysis of the time-resolved reflectivity data.

III. RESULTS AND DISCUSSION

A. Reflectivity model

Typical traces of the transient reflectivity changes ($\Delta R/R$) for the implanted and nonannealed silicon and some annealed samples are shown in Fig. 3. The data exhibit a fast rise followed by a slower recovery back toward equilibrium reflectivity. The absolute value of the maximum change in reflectivity $|\Delta R/R|$, which varies with the annealing tem-

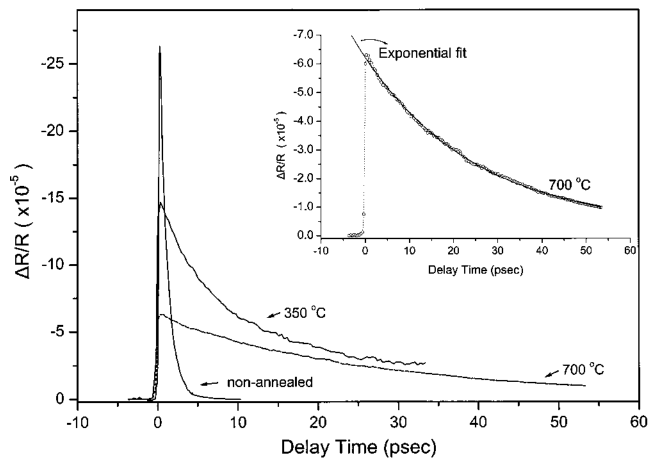

FIG. 3. Reflectivity changes for highly phosphorous implanted silicon (10^{16} P^+/cm^3). The time-resolved reflectivity response is shown for three samples: namely, for the nonannealed sample and the samples annealed at 350 and 700 °C. The upper corner graph shows the data for the 700 °C sample fitted with an exponential decay.

perature of the implanted samples, is approximately 10^{-4}. We should point out here that $|\Delta R/R|$ increased linearly with the pump beam intensity up to several times the working intensity of the experiment. The changes in reflectivity are due to an increase in the carrier density (N) and a possible rise in the temperature (ΔT). These changes are coupled to the reflectivity of the sample through the complex index of refraction $\tilde{n}$ where $\tilde{n}=n+\iota\kappa$ (n is the index of refraction, κ is the extinction coefficient, and $\iota=\sqrt{-1}$). Immediately after the laser pulse excitation the reflectivity change (ΔR) will be given by

$$\Delta R=R_0-R_1=\frac{(n_0-1)^2+\kappa_0^2}{(n_0+1)^2+\kappa_0^2}-\frac{(n_1-1)^2+\kappa_1^2}{(n_1+1)^2+\kappa_1^2}$$
$$=\frac{4\Delta n(n_0n_1-1)+4(n_1\kappa_0^2-n_0\kappa_1^2)}{[(n_0+1)^2+\kappa_0^2][(n_1+1)^2+\kappa_1^2]}, \tag{1}$$

where n_0 and κ_0 are the initial index of refraction and extinction coefficient, respectively, n_1 and κ_1 are the index of refraction and extinction coefficient following the excitation (at the maximum change), and $\Delta n=n_0-n_1$. In the above expression we have assumed near-normal incidence. For small changes in reflectivity ($\Delta R/R\ll 1$) induced by the relatively weak pulses in this work, we can approximate $n_0\approx n_1=n$ and $\kappa_0\approx\kappa_1=\kappa$ thus, the above expression may be simplified and we have

$$\frac{\Delta R}{R}\approx\frac{4\Delta n(n^2-1)+4n\Delta\kappa(2\kappa)}{[(n+1)^2+\kappa^2][(n-1)^2+\kappa^2]}. \tag{2}$$

In the case where the index of refraction is much larger than the extinction coefficient (as is true for silicon in the near-infrared region of the spectrum), the above equation is further simplified:

$$\frac{\Delta R}{R}\approx\frac{4\Delta n}{n^2-1}. \tag{3}$$

The laser-induced change in the index of refraction (Δn) has contributions from the carrier density change (Δn_N) and the temperature change ($\Delta n_{\Delta T}$). For relatively small changes we have

$$\Delta n=\Delta n_N+\Delta n_{\Delta T}=\frac{\partial n}{\partial N}\Delta N+\frac{\partial n}{\partial T}\Delta T. \tag{4}$$

A similar equation can be written for the extinction coefficient. The change due to the carrier density in the above expression may be calculated from the Drude model. According to this model, the complex dielectric function is given by

$$\tilde{\varepsilon}(\omega)=\varepsilon_R-\frac{q^2}{\varepsilon_0 m^*\omega(\omega+\iota/\tau)}N, \tag{5}$$

where ε_R is the relative dielectric constant, ε_0 is the vacuum dielectric constant, q is the electron charge, m^* the effective mass, ω is the angular frequency of the excitation electromagnetic wave, and τ is the carrier relaxation time. The dielectric function $\tilde{\varepsilon}$ is equal to the square of the complex index of refraction ($\tilde{\varepsilon}=\tilde{n}^2$). Thus, using Eq. (5) we have

$$\frac{\partial n}{\partial N}=-\frac{q^2}{2\varepsilon_0 m^*\omega^2}\left(\frac{n}{n^2+\kappa^2}\right), \tag{6}$$

$$\frac{\partial\kappa}{\partial N}=\frac{q^2}{2\varepsilon_0 m^*\omega^2}\left(\frac{\kappa}{n^2+\kappa^2}\right), \tag{7}$$

where $\omega\tau\ll 1$ (this is true for carrier time observed in these experiments). Let us consider the nonannealed implanted silicon sample used in this experiment. Taking from the literature[3,9,10] the value of optical absorption coefficient of the implanted damage layer, one can evaluate for the probing wavelength the extinction coefficient $\kappa=0.13$. The index of refraction for this sample at the probing wavelength is $n=3.35$. From Eqs. (6) and (7) we have $\Delta n_N=-7.21\times 10^{-4}$ and $\Delta\kappa_N=0.27\times 10^{-4}$.

Optical excitation of semiconductors with above band-gap photons will generate carriers. These carriers will relax through various mechanisms[7] with most of their energy transferring to the lattice (especially for indirect band-gap semiconductors like silicon). This energy transfer will raise the temperature of the lattice, resulting in a change of the refractive index through a variety of effects including shifts of the band-gap energy, electron-phonon collisions, etc. The temperature coefficients $\partial n/\partial T\sim 10^{-4}$ and $\partial\kappa/\partial T\sim 5\times 10^{-5}$ for the probing wavelength are estimated from literature[12,13] values. These values are in good agreement with photothermal experimental findings on the same set of samples[14] performed in the past. By performing a simple calculation of the energy deposited on the sample within the excitation volume and using the specific heat and density of the material, we estimate a maximum temperature rise of only $\Delta T=0.4$ K. In this calculation, the temporal aspect of the energy transfer was ignored and heat diffusion was not taken into account. Therefore, the estimated rise in temperature is the maximum possible change. Furthermore, this value will decrease for the various annealed implanted silicon samples as the penetration depth increases, thus increasing the excitation volume. Summing all the contributions for the index of refraction change due to carrier density and temperature changes we have $\Delta n=-6.81\times 10^{-4}$. Similarly for the extinction coefficient we have $\Delta\kappa=0.47\times 10^{-4}$. Using these numbers in Eq. (2), we have the maximum induced reflectivity change $\Delta R/R=-2.64\times 10^{-4}$. This value is in a very good agreement with the experimentally obtained reflectivity change for the nonannealed silicon implanted sample (see Fig. 3).

It is rather interesting to look at the contributions from the carrier density and lattice heating to the maximum change in reflectivity following an ultrafast laser pulse excitation for a broad spectrum profile covering the visible to the near-infrared region. Using the above model along with the values of the index of refraction and extinction coefficients obtained from the literature and measurements performed on the unannealed implanted sample, it was possible to calculate the change in reflectivity as a function of the wavelength of light under the same experimental conditions described in this

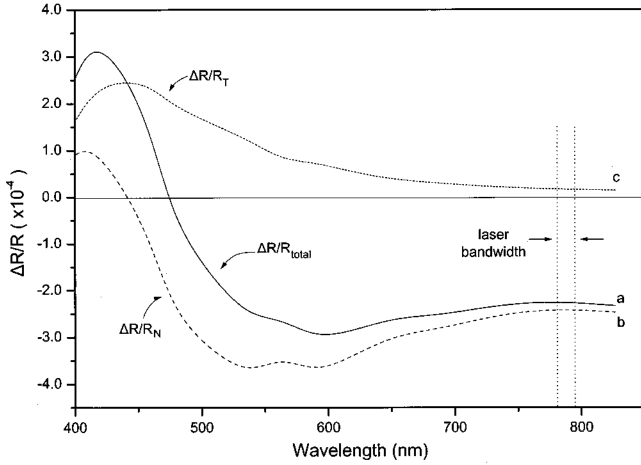

FIG. 4. Various contributions to the maximum change in the reflectivity for the $10^{16}\ \mathrm{P}^+/\mathrm{cm}^2$ implanted silicon following ultrafast laser pulse excitation vs wavelength. (a) Total contribution to the reflectivity changes from Eqs. (1) and (2). (b) Contribution from the carrier density changes. (c) Contribution from the temperature change of the lattice.

work (Fig. 4). It should be noted that the contribution from the carrier density has a positive value for wavelengths lower than 450 nm and drops below zero and remains negative for wavelengths longer than 500 nm, whereas the temperature lattice contribution is always positive. The total contribution to the change in the reflectivity at the longer wavelengths is negative and relatively constant. This relatively flat spectral profile around the region of 790 nm allowed us to neglect the spectrally broad profile (15 nm) of the ultrafast laser pulse in the calculations of the reflectivity.

B. Model for transport dynamics in silicon

The temporal aspect of the pump-probe reflectivity result will be investigated next using a mathematical model that will simulate the temporal and spatial evolution of the carrier dynamics. To model the dynamics of hot electrons and holes, a formalism is used which deals with coupled Boltzmann's equations in the relaxation time approximation for particle number, particle energy, and lattice energy.[15,16] In this model four coupled continuity equations are solved numerically for the depth- and time-dependent density N, carrier temperature T_c [the subscript c will signify carriers$\equiv e$ (electrons), h (holes)], and lattice temperature T_L. To model the reflectivity experiments in ion-implanted silicon, the formalism includes different electron and hole temperatures and also includes detailed microscopic expressions for energy exchange processes. The model, therefore, involves the solution of four coupled differential equations for the spatial and temporal dependence of N, T_e, T_h, and T_L. One can proceed from the microscopic Boltzmann equation to a macroscopic description by integrating the microscopic transport quantities over the appropriate carrier or phonon distribution functions.[15,16] For the time scales of interest and for the experimental conditions in this work we will simplify the model by assuming dependence only along the depth of the sample (z direction). In the relaxation time approximation of Boltzmann's equation one has the following relations for the electrical (j_c) and energy current (w_c) of the carriers:

$$j_c = \frac{1}{q}\sigma_c \frac{\partial \zeta_c}{\partial z} - \sigma_c Q \frac{\partial T_c}{\partial z},$$

$$w_c = \left(\Pi_c - \frac{1}{q}\zeta_c\right) j_c - \kappa_c \frac{\partial T_c}{\partial z}, \tag{8}$$

where σ_c is the electrical conductivity, Q_c is the Seebeck coefficient, Π_c is the Peltier coefficient, κ_c is the thermal conductivity, $-q$ is the charge of an electron, and ζ_c is the chemical potential of the carriers. Here we have assumed that the energy dependence of the momentum relaxation time is proportional to $(E-E_{C,V})^{-1/2}$ for lattice scattering. Under these assumptions the coefficients in Eq. (8) are simply given by

$$\sigma_c = qN\mu_m^c H_{1/2}^0(\eta_c),$$

$$Q_c = -\frac{k_B}{q_c}[\eta_c - 2H_0^1(\eta_c)],$$

$$\Pi_c = -T_c \frac{k_B}{q_c}[\eta_c - 2H_0^1(\eta_c)],$$

$$\kappa_c = -\frac{k_B^2 \sigma_c T_c}{q^2}\{6H_0^2(\eta_c) - 4[H_0^1(\eta_c)]^2\}, \tag{9}$$

where $H_j^i(\eta_c)$ is the ratio of the Fermi-Dirac integrals $F_i(\eta_c)/F_j(\eta_c)$ for reduced Fermi level η_c, μ_m^c is the mobility of carriers in a Maxwell-Boltzmann distribution, and q_c equals $-q$ for electrons and $+q$ for holes. For a laser-induced plasma the Dember field which develops due to charge separation prohibits the carrier charge and current density from becoming significantly different so that

$$j_e = -j_h, \quad N = N_e = N_h. \tag{10}$$

Given the above equations, we can write the particle current j as follows:

$$j = -D\frac{\partial N}{\partial z} - \frac{DN}{k_B[T_e H_{-1/2}^{1/2}(\eta_e) + T_h H_{-1/2}^{1/2}(\eta_h)]}\frac{\partial E_g}{\partial z} \times \frac{DN}{T_e H_{-1/2}^{1/2}(\eta_e) + T_h H_{-1/2}^{1/2}(\eta_h)} \times \left\{\left[2H_0^1(\eta_e) - \frac{3}{2}H_{-1/2}^{1/2}(\eta_e)\right]\frac{\partial T_e}{\partial z} + \left[2H_0^1(\eta_h) - \frac{3}{2}H_{-1/2}^{1/2}(\eta_h)\right]\frac{\partial T_h}{\partial z}\right\}. \tag{11}$$

The band-gap energy is given by $E_g = E_C - E_V$, and D is the ambipolar diffusion coefficient and is given by

$$D = D_e^0 D_h^0 \left\{\frac{T_e H_{-1/2}^{1/2}(\eta_e) + T_h H_{-1/2}^{1/2}(\eta_h)}{D_h^0 T_e H_0^{1/2}(\eta_c) + D_e^0 T_h H_0^{1/2}(\eta_h)}\right\}, \tag{12}$$

where $D_e^0 \propto T_e^{1/2}$ and $D_h^0 \propto T_h^{1/2}$ are the low-density electron and hole diffusion constants appropriate for the ambient lattice temperature.[17] The electron and hole energy current can be rewritten in the following form:

$$w_e = j[E_C + 2k_B T_e H_0^1(\eta_e)] - \kappa_e \frac{\partial T_e}{\partial z},$$

$$w_h = j[-E_V + 2k_B T_h H_0^1(\eta_h)] - \kappa_h \frac{\partial T_h}{\partial z}. \tag{13}$$

Similarly, the lattice current for the lattice system is given by

$$W_L = -\kappa_L \frac{\partial T_L}{\partial z}, \tag{14}$$

where κ_L is the lattice thermal conductivity. After photoexcitation, electrons and holes possess kinetic as well as bandgap energy. Therefore, one may express the total energy density for the electron (U_e) and hole (U_h) system of N carriers in the following way:

$$U_e = NE_C + \frac{3}{2} N k_B T_e H_{1/2}^{3/2}(\eta_e),$$

$$U_h = -NE_V + \frac{3}{2} N k_B T_h H_{1/2}^{3/2}(\eta_h). \tag{15}$$

The four continuity equations, which dictate the dynamics of the macroscopic variables N, T_e, T_h, and T_L, are given by

$$\frac{\partial N}{\partial t} = -\frac{\partial j}{\partial z} + Gen + Rec,$$

$$\frac{\partial U_e}{\partial t} = -\frac{\partial w_e}{\partial z} + S_e - L_e - L_{e\to h},$$

$$\frac{\partial U_h}{\partial t} = -\frac{\partial w_h}{\partial z} + S_h - L_h + L_{e\to h},$$

$$\frac{\partial T_L}{\partial t} = -\frac{\partial w_L}{\partial z}\frac{1}{C_L} + \frac{1}{C_L}\{L_e + L_h\}. \tag{16}$$

The terms L_e, L_h, and $L_{e\to h}$ appearing in the energy continuity equations are the energy transfer terms (between electrons and phonons, holes and phonons, and electrons and holes, respectively), S_e and S_h represent the energy source terms for electrons and holes, C_L is the specific heat volume ($C_L = C_V \rho$, C_V being the specific heat and ρ the density of the sample), *Rec* is the net recombination rate, and *Gen* is the carrier generation rate. The net recombination rate is given by $-\gamma N^3$, where γ is the Auger recombination coefficient and $-N/\tau$ carrier recombination through the traps induced in the silicon samples due to the ion implantation. The generation rate is taken as the following expression:

$$Gen(z,t) = \frac{\alpha I_0(t)(1-\Gamma)\exp(-\alpha z)}{\hbar\omega_0}, \tag{17}$$

where Γ is the reflectivity of the optical excitation, $I_0(t)$ is temporal profile of the intensity, $\hbar\omega_0$ is the photon energy, and α is the one-photon absorption coefficient, where contributions from two-photon absorptions are considered negligible under the present experimental conditions. The quantities S_e and S_h, which are the energy generation ratio for electrons and holes, respectively, can be calculated using conservation of energy and momentum in the absorption process from the carrier generation rate *Gen*. The total-energy-loss rate of the carriers is incorporated in the model through the use of analytic expressions for the various scattering mechanisms.[7,18,19] These include intravalley acoustic and optical phonons, intervalley acoustic and optical phonons, and electron-hole scattering. It should be noted that for the excitation wavelength used in these experiments the only valleys accessible from single-photon (phonon assisted) excitation are the X valleys. Finally the four coupled differential equations can be solved numerically with the appropriate boundary conditions:

$$\left.\frac{\partial N}{\partial z}\right|_{z=0} = \frac{s}{D} N(0,t), \quad \left.\frac{\partial T_{e,h}}{\partial z}\right|_{z=0} = 0, \quad \left.\frac{\partial T_L}{\partial z}\right|_{z=0} = 0,$$

$$N(0,z) = N_{\rm eq} \simeq 10^{12}\ \text{cm}^{-3}, \quad T_{e,h}(0,z) = 300\ \text{K},$$

$$T_L(0,z) = 300\ \text{K}, \tag{18}$$

where s is the surface recombination velocity of the samples under investigation. Initial calculations for the carrier densities and temperatures considered here have pointed out that a simplification of the above equations from using Fermi-Dirac distribution functions to a Maxwell-Boltzmann form has a negligible effect on the final results.

C. Numerical simulations

Solutions of the coupled differential equations under the experimental conditions of this work with material parameters given in Table I provide numerical simulations describing the dynamics of the photoexcited carriers. Figure 5 is one such simulation giving the time evolution of the surface values of the carrier density, temperature of the electrons and holes, and the lattice temperature for the nonannealed highly implanted silicon sample. Optical parameters such as the absorption coefficient and index of refraction were obtained from the literature and from optical and photothermal experiments performed on this set of samples. In all the numerical simulations the temporal profile of the pulse is assumed Gaussian with a full width half maximum of 80 fsec. The solid curve in the figure represents the temporal evolution of the surface carrier density of a sample with absorption coefficient 2×10^4 cm^{-1}, $n=3.35$, and $\kappa=0.13$ (values for the implanted nonannealed silicon at 790 nm). Here we have incorporated a carrier recombination term due to carrier traps generated from the implantation with a decay constant set at ~1 psec. This term was consistent with the experimentally observed recovery of the reflectivity in the pump-probe experiments. Simulations carried out with trap recombination term removed (see dotted curve in Fig. 5) were not able to account for the fast carrier density recovery. Evident from

TABLE I. Material parameters[a] of silicon and ion-implanted silicon (Refs. 2, 3, 5, 10–13, and 20–24).

Annealed temperature (°C)	κ_L [b] (W/cm K)	C_L (J K^{-1} cm^{-3})	D_e^0 (cm^2/sec)	D_h^0 (cm^2/sec)	E_g (eV)
NA	0.1	1.7	0.13	0.05	1.15
350	0.1	1.7	0.2	0.1	1.15
400	0.2	1.7	0.3	0.2	1.15
500	0.4	1.8	0.6	0.3	1.15
600	0.7	1.8	1.2	0.6	1.11
700	0.8	1.9	2.5	1.1	1.11
800	0.9	1.9	3.0	1.5	1.11
900	0.9	2.0	7	3	1.11
1000	1.1	2.0	17	5	1.11
1100	1.4	2.1	34	12	1.11

[a]Other parameters $\rho = 2.33$ g/cm^3, $\gamma = 4\times10^{-31}$ cm^6/sec, and $S < 10^4$ cm/sec.

[b]From photomodulated thermoreflectance measurements.

this simulation is the characteristic long recovery (~100 psec) consistent with carrier diffusion out of the probe region where surface recombination effects for the samples used in this work ($<10^4$ cm/sec) are considered negligible. The insert graph in Fig. 5 shows the temporal behavior of the carrier temperatures following the optical excitation. Initially, the carrier temperatures are different, which is consistent with the different energy given the two types of carriers. However, carrier collision introduced via the coupling term $L_{e\rightarrow h}$ brings the carriers at the same temperature. The carrier temperature then decreases since it loses energy to the lattice through the various mechanisms described earlier. The lattice temperature, not seen in the above graph, has approximately 0.1 °C change in its value, which is in agreement with the estimation based on a simple calculation performed earlier. Clearly, the temporal carrier density and lattice temperature profiles along with the reflectivity model described earlier provide a means for calculating the expected change in reflectivity as a function of time.

For the carrier density generated with the fluenece used in these experiments ($\sim10^{18}$ cm^{-3}) Auger recombination is considered negligible since the time constant of this recombination is calculated to be 2.5 μsec. To obtain a better understanding of the temperature-dependent ambipolar diffusion coefficient and its effects on the reflectivity measurements, we have carried out simulations with different diffusion coefficients. To isolate the diffusion effects in these simulations the trap recombination term was suppressed. The dotted line in Fig. 6 represents the situation where the diffusion coefficient is set to zero, and as expected the carrier density remains constant for the time scale of interest. The solid line corresponds to the diffusion coefficient for crystalline silicon, resulting in a time constant de-

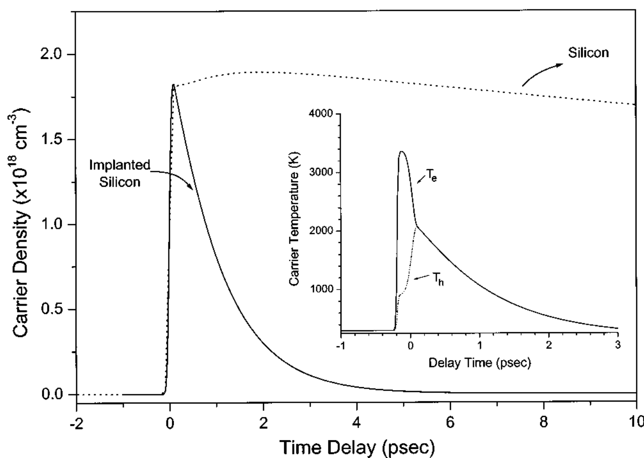

FIG. 5. Temporal profile of carrier density generated from a 80-fsec laser pulse at 790 nm, with a fluence of ~0.045 mJ/cm^2. The solid curve corresponds to the carrier density profile for ion-implanted silicon sample whose absorption coefficient is $\sim2\times10^4$ cm^{-1}. The inset represents a simulation for the carrier temperatures obtained from the model of carrier dynamics described in this work.

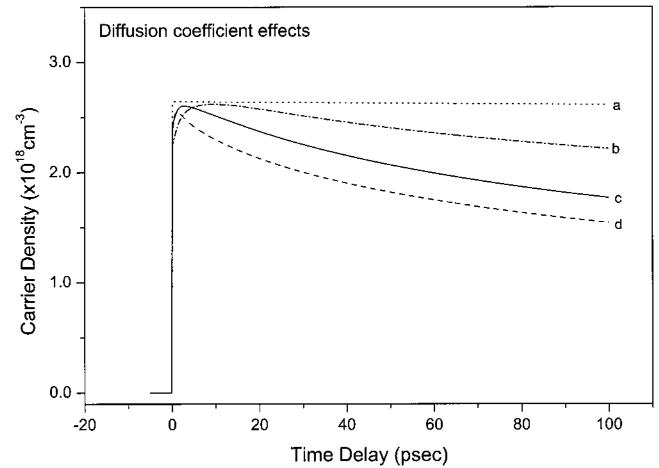

FIG. 6. Effects of the temperature-dependent ambipolar diffusion on the carrier density generated from a 80-fsec laser pulse at 790 nm, with a fluence of ~0.045 mJ/cm^2. (a) The dotted curve corresponds to the carrier density profile with zero diffusion coefficient. The other curves correspond to (b) 0.1 times the crystalline silicon diffusion coefficient, (c) the crystalline silicon diffusion coefficient, and finally (d) 2.0 times the crystalline silicon diffusion coefficient.

cay of ~100 psec. This is in agreement with the time constant measured from the time-resolved reflectivity for crystalline silicon and for the 1100 °C–annealed ion-implanted silicon. Other values for diffusion coefficient were also chosen in an attempt to obtain a clear understanding of the reflectivity changes observed in the pump-probe experiments. Clearly, the fast recovery of the nonannealed silicon and the lower annealed samples could not be explained due to carrier diffusing out of the probing region, as one would expect the diffusion to decrease with increasing disorder due to implantation.

D. Fitting and analysis of experimental results

The time evolution of the change in reflectivity as seen in the experimental data presented in Fig. 3 is consistent with a pulse-width-limited rise and an exponential recovery. In view of the fact that the pulse is extremely short in duration, compared to the recovery of the reflectivity, the time constant of the decay may be extracted by fitting a simple exponential decay to the data. In an attempt to obtain a better fit to the experimental data and explain their temporal behavior, the carrier kinetics model is used in conjunction with the reflectivity model to simulate the changes in observed reflectivity. The two most important fitting parameters to these simulations were the absorption coefficient and the trap recombination time constant. All parameters used in these simulations are experimentally obtained and/or obtained from the literature (see Table I). The TEM measurements suggest that the nonannealed sample consist of a thin amorphous layer followed by crystalline silicon with a well-defined amorphous-crystalline interface. Similarly, for the lower-temperature-annealed samples there is a thin amorphous layer followed by crystalline silicon. Hence the reflectivity signal for the lower-temperature-annealed samples comes essentially from the amorphous layer, since the signal from the crystalline silicon is very small due to the large penetration depth. This is also supported by the fact that a single decay component was observed in the time-resolved reflectivity data. At higher temperatures (>500 °C) the amorphous layer is completely annealed: however, defects and dislocation are still present. This is evident from the observed different values of the carrier lifetime and reflectivity signal as a function of annealing temperature.

Figure 7 shows the calculated and experimental time-resolved reflectivity of the nonannealed (a) and annealed at 700 °C (b) ion-implanted silicon. The squares are the experimental time-resolved reflectivity data obtained at 790 nm for a fluence of 0.045 mJ/cm^2. The solid curve represents the calculated reflectivity change. Best-fit results for the nonannealed sample were obtained with an absorption coefficient of 2.34×10^4 cm^{-1} and trap recombination time $\tau_r=0.97$ psec, whereas for the sample annealed at 700 °C a best fit was obtained with an absorption coefficient of 0.5×10^4 cm^{-1} and recombination time $\tau_r=29.3$ psec. The absorption coefficient values are consistent with expected value for highly implanted silicon.[2,3,9,10] Similar simulations were carried out for all the annealed ion-implanted silicon samples. In all simulations the calculated changes in reflectivity were fitted against the experimental reflectivity results. The resulting best-fit parameters for all the samples are given in Table II. The relative fast recovery of the reflectivity of the silicon samples is attributed to the high density of traps introduced by ion implantation. This is in agreement with previous published work on carrier lifetimes on ion-implanted silicon on sapphire.[4] What is rather interesting in the data is the behavior of the carrier lifetime as a function of the annealing temperature.

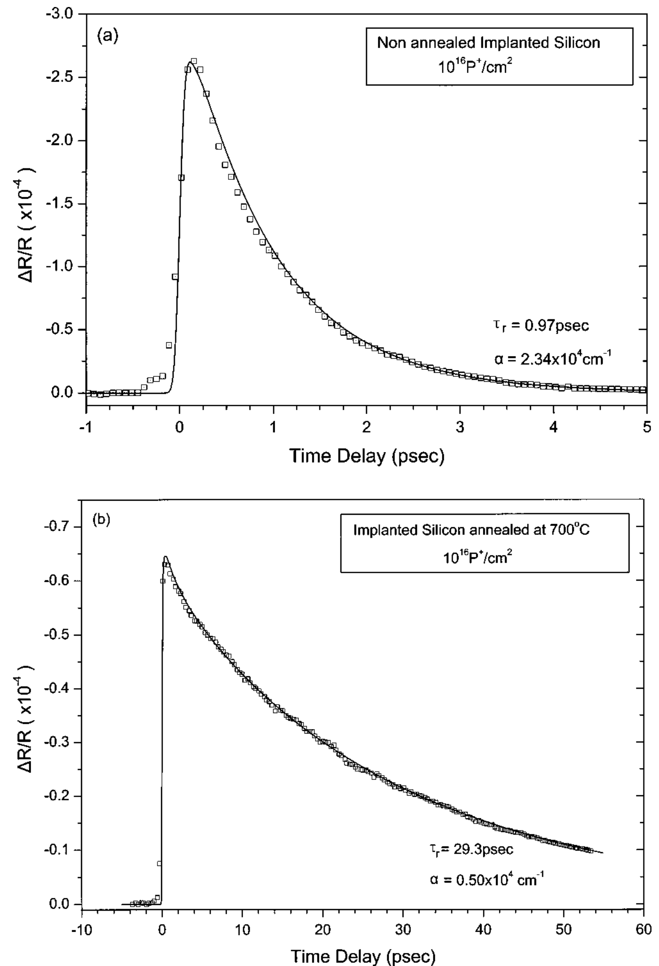

FIG. 7. Time-resolved reflectivity of the (a) nonannealed and (b) annealed at 700 °C ion implanted silicon (10^{16} P$^+$/cm^2) at 790 nm for a fluence of 0.045 mJ/cm^2. The squares are experimental data for and the solid curve is calculated reflectivity changes from the simulations of the carrier density and lattice temperature.

Figure 8 shows the carrier lifetimes obtained from fitting the simulation results to the time-resolved reflectivity data as a function of the annealing temperatures of the implanted silicon samples (see Table II). As expected, the carrier lifetime appears to increase with higher annealing temperature since the recombination traps are removed. However, it is interesting to note a decrease in lifetime at specific points of annealing: namely, at 500 and 900 °C. In fact, as was shown in the past on the same set of samples at 500 °C, the phenomenon of "negative annealing" appears due to the formation of complex clusters. These clusters disappear for higher annealing. Around 900 °C one can point out the pres-

TABLE II. Time-resolved measurements data and fitted results from simulations.

Annealing temperature (°C)	Peak $\Delta R/R$ ($\times 10^{-4}$) (Experimental value)	Carrier lifetime (psec)	α ($\times 10^4$ cm^{-1})
NA	2.71	0.97	2.34
350	1.49	8.9	1.28
400	1.10	18.4	0.95
500	0.88	11.9	0.80
600	0.71	16.6	0.56
700	0.62	29.3	0.50
800	0.59	41.1	0.44
900	0.27	19.6	0.23
1000	0.17	29.4	0.11
1100	0.08	95	0.09

ence of dislocation lines and loops. These dislocations require anneals up to 1100 °C in order to be removed completely. The signs of these phenomena are clearly present on the experimental values presented in the figure. Similar results concerning the negative annealing have also been observed in the past on the same series of samples.[8,25–27]

Although the transient reflectivity signal for the 1100 °C–annealed sample was very weak (due to the large penetration depth and thus smaller change carrier density and therefore smaller change in reflectivity), we have estimated the carrier lifetime to be approximately 95 psec. This is in good agreement with the time-resolved measurements reported in the literature for crystalline silicon (~100 psec), suggesting that the highly annealed sample has fully recovered its crystallinity with all the recombination traps removed. The recovery of the sample annealed at 1100 °C is also demonstrated from the Raman scattering data seen in Fig. 9. As seen in Fig. 9(a), the characteristic phonon mode at 64.6 meV is not visible for the nonannealed sample where in its place there is a broadband feature indicative of the amorphous nature of the silicon sample. With increasing annealing temperature the phonon peak increases in height, reaching its maximum at the highest annealing temperature [Fig. 9(b)], which is the same as the Raman signal for crystalline silicon. Since the Raman probing wavelength is very close to the wavelength used in the time-resolved experiments to a first approximation, we may use the phonon peak of the Raman scattering data for each of the samples as a means of estimating how much of the probed sample is crystalline and how much is amorphous.

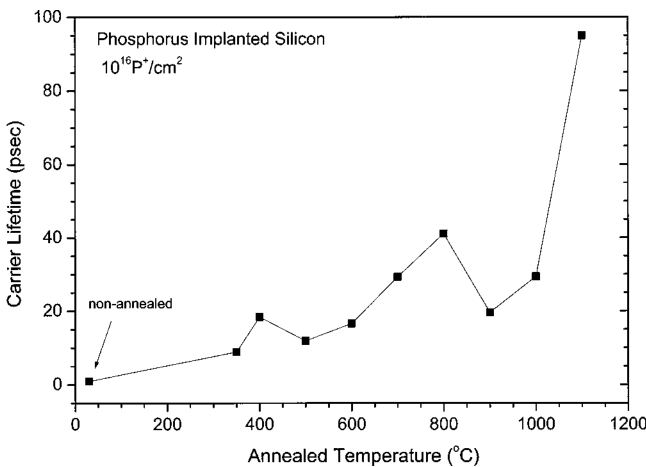

FIG. 8. Carrier lifetimes as a function of annealed temperature obtained from fitting the time resolved data to simple exponential decays.

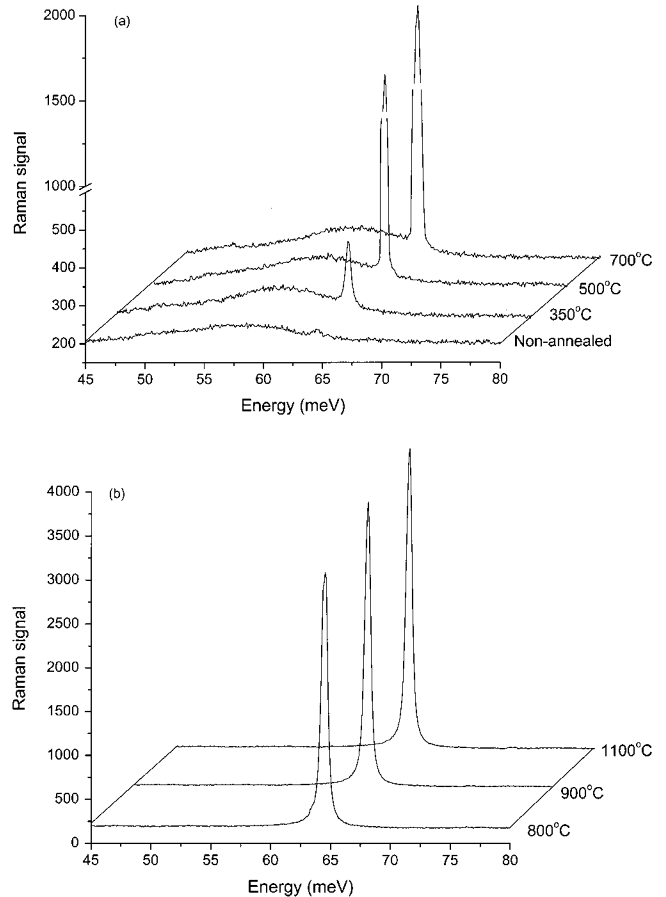

FIG. 9. Raman scattering data (at 752.5 nm) for the implanted silicon samples at various annealing temperatures. The characteristic Raman phonon line at 64.6 meV is clearly seen in annealed samples. The nonannealed sample exhibits a broadband feature, which becomes more localized with increasing annealing temperature.

One of the properties of the near-infrared laser wavelength used in the experiment is the relatively long penetration depth (10 μm) of excitation and probing beams for crystalline silicon. Unfortunately, ion implantation changes drastically this depth, and to further complicate matters, this is also strongly affected by the temperature of annealing. The penetration depth is directly related through the photogenerated carrier density to the change in the amplitude of the reflectivity signal. With increasing penetration depth the excitation volume increases in length, while the number of photoexcited carriers remains the same, as the energy density is constant. This in effect decreases the carrier density, thus resulting in a smaller reflectivity signal. This is clearly seen

from the data presented in Table II where, in addition to the carrier lifetime, the respective peak reflectivity change for all the annealed implanted silicon samples is presented.

The shortest carrier lifetime measured was for the nonannealed sample. This is expected since the nonannealed sample will have the maximum defect formation from the implantation and thus the largest number of recombination traps, allowing for faster relaxation of the photoexcited carriers. The extent of the implantation damage can be clearly seen from the Raman scattering data in Fig. 9. Furthermore, the nonannealed sample has the smallest penetration depth from all the samples due to the largest absorption coefficient generated from the implantation-induced 0.55-μm amorphous layer observed by the TEM measurements. This is clearly demonstrated by the largest value of the peak change in the reflectivity (see Table II).

The annealing process of the implanted silicon, even as low as 350 °C, induces a great deal of change in the carrier lifetime. The lifetime of the photogenerated carriers increased to 8.9 psec as the recombination traps are annealed and removed. This takes place thanks to the annihilation of point defects. At the same time the optical penetration depth is expected to increase, resulting in a decrease of the photoexcited carrier density in the probing region and, thus, a noticeable decrease in the amplitude reflectivity change appears. The carrier lifetime increases further with increasing the annealing temperature to 400 °C, whereas the signal is decreasing. The drop in carrier lifetime at the 500 °C sample discussed earlier is believed to be due to the formation of complex clusters as the implanted samples are annealed, the impurities diffuse into the bulk forming clusters, which act as recombination center and traps to the photogenerated carriers. This clustering, however, is not evident from the Raman scattering data. As is well known, around 700 °C we have annihilation of complex defects resulting in an increase of carrier lifetime, as is evident from the data in Fig. 8. Nevertheless, at higher annealing temperatures (900 °C) dislocation lines and loops become an important recombination mechanism for the carriers generated following ultrafast-pulse photoexcitation, which results in a decrease in carrier lifetime. A further increase in the annealing temperature removes the dislocation lines and loops, resulting again in an increase in carrier lifetime. Specifically, a change of annealing temperature from 900 to 1100 °C results in an increase of carrier lifetime from 19.6 to 95 psec.

The absorption coefficients for all the annealed implanted silicon samples obtained from fitting simulation data to the time-resolved reflectivity measurements are plotted in Fig. 10. These fitted parameters are strongly dependent on the amplitude of the reflectivity signal, which clearly depends on the intensity of the laser excitation. Repeated measurements with the same samples gave an estimate of the error of the signal, which was approximately ±5%. This was also the estimated error in the effective optical absorption coefficient obtained from the simulations of each sample. The values of optical absorption coefficients obtained for all samples are in good agreement with results presented in the literature.[3] In fact, as expected, the highest absorption coefficient α is obtained for the nonannealed sample. For this sample, since the penetration depth is smaller than the amorphous layer (<0.55 μm), the entire incident light is absorbed with in the implanted layer. We should note here that the optical absorption coefficient decreases drastically even after temperature annealing at 350 °C. These changes are mainly due to the relaxation of the amorphous structure from the annihilation of point defects and redistribution of impurities from interstitial to substitutional sites. At higher temperature annealing (400 and 500 °C) there is a further decrease in the absorption coefficient, which is believed to be due to additional relaxation of the amorphous phase. Annealing at higher temperatures removes completely the amorphous layer as was observed by the TEM measurements [see Figs. 2(a)–2(c)], resulting in a further decrease of the absorption coefficient. The same phenomena were also observed in the past by other researchers.[2,28,29] In the annealing region between 600 and 800 °C one can observe that the variation of optical absorption coefficient is relatively small. This is in good agreement with other measurements, performed by our group on the set of samples, and is believed to be due to certain rearrangements of the disorder.[8,26,30] At 900 °C, α decreases by a factor of 2 and this is in good agreement with the annihilation of defects and amorphous clusters in the crystalline matrix. Annealing at higher temperature, such as 1000 °C, leads to the annihilation of dislocation lines and loops, a fact which explains the further decrease of the optical absorption coefficient.

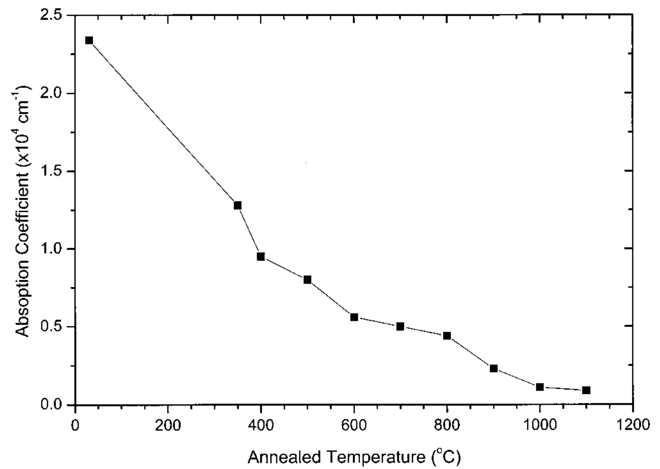

FIG. 10. Absorption coefficients for the entire annealed ion-implanted silicon samples obtained from fitting the time-resolved measurements to simulations.

IV. CONCLUSIONS

Carrier dynamics in highly implanted silicon samples and annealed at various temperatures have been investigated using time-resolved reflectivity measurements along with a mathematical self-consistent kinetic model based on the Boltzmann transport equation. Carrier lifetimes as short as 0.97 psec for the highly implanted nonannealed sample have been recorded. Although the carrier lifetime appears to be increasing with annealing temperature, there can be identified two specific annealing temperature points where there is

a decrease in the lifetime of the carriers. This behavior was attributed to cluster formations and line dislocations and loops acting as recombination centers. Although Raman scattering data indicate that at annealing temperatures over 900 °C the implanted silicon has become crystalline, transient reflectivity data indicate that defects that are present, even following annealing at such high temperatures, act as recombination centers for the photoexcited carriers resulting in lifetimes, which are shorter than expected. A complete recovery of the ionimplanted silicon with carrier lifetimes measuring >95 psec occurs at annealing temperatures over 1100 °C.

ACKNOWLEDGMENTS

This work has been supported by the Research Promotion Foundation of the Government of Cyprus under Contract No. I.Π.E 4°, 42/2001. Special thanks go to Professor J. Stoemenos from the Physics Department of the Salonica University (Greece) for the TEM measurements.

*Electronic address: othonos@ucy.ac.cy

[1] H. Ryssel and I. Ruge, *Ion Implantation* (Wiley, Toronto 1986).
[2] *Effect of Disorder and Defects in Ion-Implanted Semiconductors: Electrical and Physiochemical Characterization*, Vol. 45 of *Semiconductors and Semimetals*, edited by G. Ghibaudo and C. Christofides (Academic, New York, 1997).
[3] *Effect of Disorder and Defects in Ion-Implanted Semiconductors: Optical and Photothermal Characterization*, Vol. 46 of *Semiconductors and Semimetals*, edited by C. Christofides and G. Ghibaudo (Academic, New York, 1997).
[4] J. Kubhl, E. O. Gobel, Th. Pfeiffer, and A. Jonietz, Appl. Phys. A: Solids Surf. **34**, 105 (1984).
[5] O. B. Wright, U. Zammit, M. Marinelli, and V. E. Gusev, Appl. Phys. Lett. **69**, 553 (1996).
[6] F. E. Doany, D. Grischkowsky, and C. C. Chi, Appl. Phys. Lett. **50**, 460 (1987).
[7] A. Othonos, Appl. Phys. Rev. **83**, 1789 (1998).
[8] A. Othonos, C. Christofides, J. Boussey-Said, and M. Bisson, J. Appl. Phys. **75**, 8032 (1994).
[9] U. Zammit, K. N. Madhusoodanan, M. Marinelli, F. Scudieri, R. Pizzoferrato, F. Mercuri, E. Wendler, and W. Wesch, Phys. Rev. B **49**, 14 322 (1994).
[10] D. E. Aspnes, A. A. Studna, and E. Kinsbron, Phys. Rev. B **29**, 768 (1984).
[11] D. E. Aspnes and A. A. Studna, Phys. Rev. B **27**, 985 (1983).
[12] G. E. Jellison and F. A. Modine, Phys. Rev. B **27**, 7466 (1983).
[13] G. E. Jellison and F. A. Modine, Appl. Phys. Lett. **41**, 180 (1982).
[14] M. Nestoros, B. C. Forget, C. Christofides, and A. Seas, Phys. Rev. B **51**, 14 115 (1995).
[15] H. M. van Driel, Phys. Rev. B **35**, 8166 (1987).
[16] A. Othonos, H. M. van Driel, J. F. Young, and P. J. Kelly, Phys. Rev. B **43**, 6682 (1991).
[17] J. F. Young and H. M. van Driel, Phys. Rev. B **26**, 2147 (1982).
[18] E. M. Conwell, in *Solid State Physics*, edited F. Seitz, D. Tumbull, and H. Ehrenreich (Academic, New York, 1967), Suppl. 9.
[19] C. Jacoboni and L. Reggiani, Rev. Mod. Phys. **55**, 645 (1983).
[20] R. F. Wood and G. E. Giles, Phys. Rev. B **23**, 2923 (1981).
[21] J. Dwiezor and W. Schmid, Appl. Phys. Lett. **31**, 346 (1977).
[22] S. M. Sze, *Physics of Semiconductor Devices* (Wiley, New York, 1969).
[23] J. Geist and W. K. Gladden, Phys. Rev. B **27**, 4833 (1983).
[24] R. Reitano, M. G. Grimaldi, P. Baeri, E. Bellandi, S. Borghesi, and G. Baratta, J. Appl. Phys. **74**, 2850 (1993).
[25] A. Othonos, C. Christofides, and A. Mandelis, Appl. Phys. Lett. **69**, 821 (1996).
[26] A. Seas, M. Eleftheriou, C. Christofides, and C. R. Theocharis, Nucl. Instrum. Methods Phys. Res. B **103**, 46 (1995).
[27] A. Othonos and C. Christofides, J. Appl. Phys. **78**, 796 (1995).
[28] J. Boussey-Said, G. Ghibaudo, J. Stoemenos, and P. Zaumseil, J. Appl. Phys. **72**, 61 (1992).
[29] L. Csepredgi, E. F. Kennedy, T. J. Gallager, J. W. Mayer, and T. W. Sigmon, J. Appl. Phys. **48**, 4234 (1977).
[30] A. Othonos and C. Christofides, J. Appl. Phys. **78**, 796 (1995).